J. Fluid Mech. (1987), *vol.* 181, *pp.* 233–263
Printed in Great Britain

Nonlinear response of a rotating fluid to differential heating from below

By CHARLES QUON

Atlantic Oceanographic Laboratory, Department of Fisheries and Oceans, Bedford Institute of Oceanography, Dartmouth, N.S., Canada B2Y 4A2 and National Center for Atmospheric Research, Boulder, CO 80303, USA

(Received 17 July 1985 and in revised form 30 July 1986)

This paper studies numerically the instabilities and quasi-steady states of thermal convection in a Boussinesq fluid within a unit square which is bounded rigidly on all sides, differentially heated on the bottom, insulated above, and rotating about a vertical axis. The flows for five ascending values of the thermal Rossby number β are studied for constant Prandtl number σ and infinitesimal Ekman number E. For small values of β, either transient or stationary spatial oscillations occur. The results agree with Daniels' (1976) and Daniels & Stewartson's (1977, 1978) linear and weakly nonlinear theories in principle if not in detail. For large values of β, the flows are highly nonlinear. They undergo two distinct stages of instability and eventually settle down to steady states. It is shown that a viscous non-diffusive boundary layer can exist at steady state for large β. For the maximum value of β under investigation, only quasi-steady states have been reached in the interior. Inertial gravity waves are observed emanating from the unstable corner of the fluid. These numerical solutions establish that the initial instability is an exchange instability rather than a catastrophic one. The question of bifurcation has not been resolved.

1. Introduction

Daniels (1976) and Daniels & Stewartson (1977, 1978) (hereinafter referred to as D & S), investigated analytically the axisymmetric motion of a rigidly bounded rotating annulus heated differentially on the bottom while all the upper boundaries are thermally insulated. These authors extensively investigated the flows for infinitesimal Ekman number E, for small thermal Rossby number β, and for Prandtl number σ of order unity or larger (these parameters will be defined below). They found that for vanishingly small thermal Rossby number, heat transport in the interior is by conduction. The resulting circulation in the meridional (cross-sectional) plane consists of $E^{\frac{1}{4}}$ Ekman layers near the top and bottom boundaries, $E^{\frac{1}{3}}$ Stewartson–Proudman layers on the vertical sidewalls, and small but uniform vertical flows in the interior. As the thermal Rossby number increases, the $E^{\frac{1}{4}}$ layer in the hot side of the fluid becomes spatially oscillatory. It does not decay with distance from the boundary; instead, it penetrates into the interior in the form of cellular motion which can be interpreted as Bénard convection. The problem, however, is much more complicated than the classical Bénard problem. For example, because the container is tall, the convection cells can have multiple vertical wavenumbers. In addition, non-uniform heating in the horizontal always maintains some non-trivial state of motion which makes this problem fundamentally different from the Bénard problem whose basic state is one of no motion.

Hignett, Ibbetson & Killworth (1981) studied the problem experimentally. Unfortunately, they did not report on the transient flows. However, in spite of the differences between the boundary conditions applied in their experiments and in our computations, our numerical solutions presented below agree, at least qualitatively, with their observations on the steady states. The authors of all these studies have discussed certain similarities between the flows of the present problem and those of some large-scale geophysical phenomena such as zonally averaged oceanic and planetary atmospheric circulations. A similar convection problem without rotation, which was studied by Stommel (1962), by Rossby (1965), and later by Killworth & Manins (1980), was indeed motivated by the question of small sinking regions in the world oceans.

Some related problems have also been studied numerically on both planetary and laboratory scales. Beardsley & Festa (1972) studied the flows in a similar, but non-rotating configuration with an impressed surface stress. Kalnay de Rivas (1973) had studied a hydrostatic model of the zonally averaged Venusian atmosphere. Although her model is very similar to the present one, the hydrostatic assumption in her model deprived her study of much of the intricate and interesting flow phenomena that are inherent in this problem. Quon (1980, 1981) studied a more complex problem with both the upper and lower boundaries differentially heated. In retrospect, many aspects of the transient behaviour of that problem are very similar to what is to be described below. The present work is indeed a logical outgrowth of these earlier studies.

In this paper, we shall focus on the fundmentals of various modes of motion in the system rather than on its possible geophysical applications. As we shall see, the richness of its full range of phenomena justifies a rigorous fluid-dynamical study. We shall first define the problem, then briefly review the method of solution and some previous works. The numerical results will then follow. This study covers a wide range of thermal Rossby numbers. The Prandtl number is kept constant while the Ekman number kept small.

2. Statement of the problem

The physical system consists of a unit square as depicted in figure 1, which can be considered as the cross-section of an infinite channel, or that of an annulus of fluid with negligible annulus gap to radius ratio. The upper boundaries of the square are rigid and thermally insulated. The bottom boundary is maintained at temperatures varying with distance from the sidewalls. The whole system rotates about a vertical axis. We shall impose a Cartesian coordinate $\boldsymbol{X} = (x, y, z)$ as shown in figure 1, and designate a velocity vector $\boldsymbol{V} = (u, v, w)$. After non-dimensionalization with characteristic velocity $U = 2\Omega L$, length L, and temperature ΔT, where Ω is the rotation rate, L the width and height of the square cross-section, and ΔT the maximum imposed temperature difference, the two-dimensional governing equations are

$$\frac{\partial u}{\partial t} + u\frac{\partial u}{\partial x} + w\frac{\partial u}{\partial z} - v = -\frac{\partial p}{\partial x} + E\nabla^2 u, \tag{2.1}$$

$$\frac{\partial v}{\partial t} + u\frac{\partial v}{\partial x} + w\frac{\partial v}{\partial z} + u = E\nabla^2 v, \tag{2.2}$$

$$\frac{\partial w}{\partial t} + u\frac{\partial w}{\partial x} + w\frac{\partial w}{\partial z} = -\frac{\partial p}{\partial z} + \beta T + E\nabla^2 w, \tag{2.3}$$

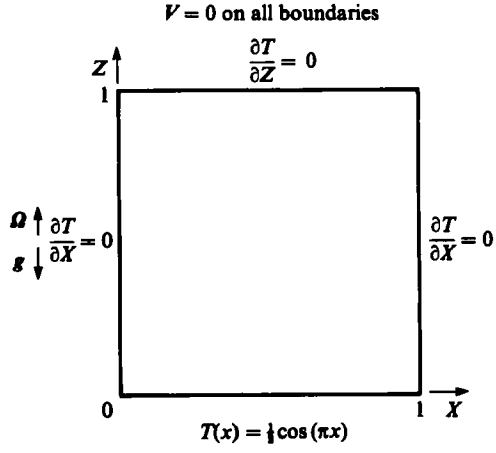

FIGURE 1. The physical system and boundary conditions.

$$\frac{\partial T}{\partial t}+u\frac{\partial T}{\partial x}+w\frac{\partial T}{\partial z}=\frac{E}{\sigma}\nabla^2 T, \tag{2.4}$$

$$\text{div } V=0, \tag{2.5}$$

with the following boundary conditions:

$$\left.\begin{aligned} V&=0 \quad \text{on all boundaries,}\\ \frac{\partial T}{\partial n}&=0 \quad \text{on all boundaries except the bottom,}\\ T&=T(x)=\tfrac{1}{2}\cos\pi x \text{ on the bottom,}\end{aligned}\right\} \tag{2.6}$$

where $\partial/\partial n$ denotes the normal gradient on the boundaries. The dimensionless parameters are

$$E=\frac{\nu}{2\Omega L^2} \quad \text{Ekman number,} \tag{2.7a}$$

$$\beta=\frac{\alpha g\Delta T}{4\Omega^2 L} \quad \text{Thermal Rossby number,} \tag{2.7b}$$

$$\sigma=\frac{\nu}{\kappa} \quad \text{Prandtl number,} \tag{2.7c}$$

where ν and κ are respectively the kinematic viscosity and thermal diffusivity, α the coefficient of volumetric expansion, and g the Earth's gravity. An external Rayleigh number can be defined as follows:

$$Ra=\frac{\alpha g\Delta T/H}{\kappa\nu}L^4=\sigma\beta E^{-2}. \tag{2.8a}$$

Note that Ra is based on an externally imposed vertical temperature gradient $\Delta T/H$ and an external lengthscale L. We shall have to consider an internal Rayleigh number Ra defined as

$$Ra_i=Ra\left|\frac{\partial T}{\partial z}\right|l^4, \tag{2.8b}$$

Case	β	$Ra\left(L, \frac{\Delta T}{H}\right) = \sigma\beta E^{-2}$	$Ra\left(l, \frac{\Delta T}{H}\right) = \sigma\beta E^{-2} l^4$	Minimum vertical temperature gradient for instability according to either (4.5) or (4.6)				Γ_{max}	Γ_{min}	Ψ_{max}
				$n = 1$	$n = 2$	$n = 3$	$n = 4$			
1	1.0×10^{-3}	2.777×10^{4}	3.542	5.995	15.105	25.937	38.063	2.528×10^{-4}	-2.043×10^{-4}	4.635×10^{-6}
2	5.0×10^{-3}	2.222×10^{6}	4.463×10	4.910×10^{-1}	1.237	2.124	3.117	1.013×10^{-3}	-8.137×10^{-4}	7.121×10^{-6}
3	2.0×10^{-2}	8.888×10^{6}	1.785×10^{2}	1.227×10^{-1}	3.093×10^{-1}	5.311×10^{-1}	7.794×10^{-1}	4.032×10^{-3}	-2.756×10^{-3}	3.080×10^{-5}
4	2.0×10^{-1}	8.888×10^{7}	1.785×10^{3}	1.227×10^{-2}	3.093×10^{-2}	5.311×10^{-2}	7.794×10^{-2}	1.552×10^{-2}	-1.507×10^{-2}	$.419 \times 10^{-4}$
5	1.0	4.444×10^{8}	8.926×10^{3}	2.455×10^{-3}	6.186×10^{-3}	1.062×10^{-2}	1.559×10^{-2}	4.243×10^{-2}	-4.404×10^{-2}	5.357×10^{-4}

TABLE 1. Parameters of computation and estimate of minimum vertical temperature gradient for vertical wavenumber n instability; $\sigma = 10, E = 6 \times 10^{-4}$ for case 1 and $E = 1.5 \times 10^{-4}$ for all other cases. $l = (2E)^{\frac{1}{2}}$ as in D & S.

where $\partial T/\partial z$ is a typical dimensionless internal vertical temperature gradient and l some dimensionless internal lengthscale. Note that both these quantities depend implicitly on the rotation rate and some other parameters of the system. Thus Ra_1 in (2.8*b*) depends on Ω, although Ra in (2.8*a*) does not.

In this study the Ekman number will be kept small, $O(10^{-4})$, and $\sigma = 10$ and β will vary from infinitesimal to $O(1)$. Small E ensures a geostrophic interior. The parameters of five case studies are given in table 1.

3. Method of solution

Equations (2.1)–(2.6) have been solved by a finite-difference method on a transformed coordinate. The transformation has been chosen such that there are more grid points in the boundary region where the fields vary more rapidly than in the interior. The advantage of using transformed coordinates instead of other methods of mesh refinement is that the transform function can be changed at will to suit the requirement of each problem. For example, the same general algorithm used here for side-boundary-layer computation can be used to study internal boundary layers just by changing the transform function to yield grid refinement in the interior instead of the sidewalls. The disadvantage is that we have to solve a set of much more complicated equations where the spatial derivatives are replaced by derivatives in the transformed space with known, but nevertheless variable, coefficients. The essence of the method is as follows.

With the transformation $x \to \xi(x), z \to \eta(z)$, (2.1)–(2.5) become

$$\frac{\partial u}{\partial t} + \boldsymbol{V} . \boldsymbol{A} u - v = -\frac{\partial \xi}{\partial x}\frac{\partial p}{\partial \xi} + ELu, \tag{3.1}$$

$$\frac{\partial v}{\partial t} + \boldsymbol{V} . \boldsymbol{A} v + u = +ELv, \tag{3.2}$$

$$\frac{\partial w}{\partial t} + \boldsymbol{V} . \boldsymbol{A} w = -\frac{\partial \eta}{\partial z}\frac{\partial p}{\partial \eta} + ELw + \beta T, \tag{3.3}$$

$$\frac{\partial T}{\partial t} + \boldsymbol{V} . \boldsymbol{A} T = \frac{E}{\sigma} LT, \tag{3.4}$$

$$\boldsymbol{A} . \boldsymbol{V} = 0, \tag{3.5}$$

where

$$\boldsymbol{A} = \hat{\boldsymbol{i}}\frac{\partial \eta}{\partial x}\frac{\partial}{\partial \eta} + \hat{\boldsymbol{k}}\frac{\partial \xi}{\partial z}\frac{\partial}{\partial \xi}, \quad L = \boldsymbol{A} . \boldsymbol{A}.$$

A diagnostic pressure equation is formed by operating on (3.1) with $(\partial \eta/\partial x)(\partial/\partial \eta)$ and on (3.3) with $(\partial \xi/\partial z)(\partial/\partial \xi)$ and adding the resulting equations:

$$Lp = -\frac{\partial}{\partial t}\boldsymbol{A} . \boldsymbol{V} + Q(u, v, w, t), \tag{3.6}$$

where $Q(u, v, w, t)$ consists of the rest of the terms in (3.1) and (3.3) after differentiation.

Equation (3.6) is elliptic with variable coefficients. Although $\boldsymbol{A} . \boldsymbol{V} = 0$ is assumed in differential form, it does not vanish completely in finite-difference form because of truncation errors. Hence the first term in the right-hand side of (3.6) is non-zero, and unfortunately is also unknown because the time derivative requires $\boldsymbol{A} . \boldsymbol{V}$ of the

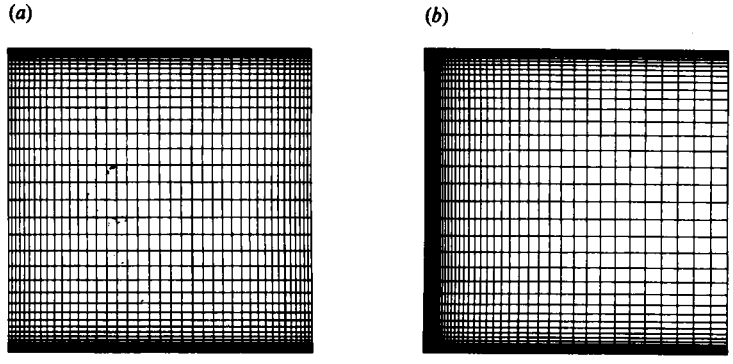

FIGURE 2. Symmetric and asymmetric grid distributions. The parameter $d = 0.02$ for symmetric transformation in the vertical for (a) and (b); $d = 0.15$ for symmetric transformation in the horizontal (a), and $d = 0.05$ for the asymmetric transformation (b). The nets consist of 42×42 grid points.

next time level. As the best approximation, $\boldsymbol{A} \cdot \boldsymbol{V}$ in the future time-step is forced to be zero in the computation for p in (3.6). A detailed exposition of the finite-difference procedure is given in Quon (1976). The same algorithm used for numerical computation here has been used to solve a few rotating and non-rotating convection problems successfully (Quon 1976, 1977, 1980, 1981, 1983a).

Two-different transform functions have been used respectively for infinitesimal and large β. When β is infinitesimal, the flow fields and temperature field are either symmetric or antisymmetric about $x = \frac{1}{2}$, and hence a symmetric transform function is used for the horizontal-coordinate transform. For larger values of β, the flow fields have a very narrow and intense boundary layer on only one vertical boundary. Hence a transform function that is symmetric about $x = 1$ and has fine grids near $x = 0$ is used in the horizontal direction. Symmetric vertical transform functions are used for all cases because Ekman layers are expected near both the upper and lower boundaries. These transform functions are respectively

(a) symmetric

$$\xi(x) = \tfrac{1}{2}(N+1)+\tfrac{1}{2}(N-1)\frac{\ln[(b+x-0.5)/(b-x+0.5)]}{\ln[(b+0.5)/(b-0.5)]},$$

$$b^2 = \frac{0.25}{1-2d}, \quad 0 \leqslant x \leqslant 1;$$

(b) asymmetric

$$\xi(x) = N+(N-1)\frac{\ln[(b+x-1)/(b-x+1)]}{\ln[(b+1)/(b-1)]},$$

$$b^2 = \frac{1}{1-d}, \quad 0 \leqslant x \leqslant 1,$$

where d is a controlling parameter. For convenience, N and ξ are chosen to be integers and $1 \leqslant \xi \leqslant N$ for $0 \leqslant x \leqslant 1$. The smaller d is, the more grid points are packed into the boundary layers. Two examples are given in figure 2. A detailed discussion of the symmetric transformation function is given in Roberts (1971) and Quon (1976). Since the asymmetric transform function is essentially an adaptation of the symmetric function to a special circumstance, these discussions apply to both.

The finite-difference scheme is second-order accurate in space and in time. Because of non-uniform grid spacings, the truncation errors are necessarily non-uniform in space. As we shall see later, it is very difficult to assess the absolute accuracy of the solutions for a problem as complex as the present one. The algorithm used to produce the results presented here has been severely tested in some other areas of study (Quon 1976, 1983*a*).

4. Results of linear and weakly nonlinear theories

If β is sufficiently small, it is convenient to scale the velocity with $2\Omega L\beta$. Neglecting the inertial terms that are $O(\beta^2)$, and introducing a stream function Ψ such that $u = -\partial\Psi/\partial z$, and $w = \partial\Psi/\partial x$ we can obtain the following from (2):

$$\frac{\partial v}{\partial z} = \frac{\partial T}{\partial x} + E\nabla^4\Psi, \tag{4.1}$$

$$\frac{\partial \Psi}{\partial z} = E\nabla^2 v, \tag{4.2}$$

$$\sigma\beta\left(-\frac{\partial\Psi}{\partial z}\frac{\partial T}{\partial x} + \frac{\partial\Psi}{\partial x}\frac{\partial T}{\partial z}\right) = E\nabla^2 T. \tag{4.3}$$

If $\sigma\beta$ is also sufficiently small, the left-hand side of (4.3) can be neglected for the lowest-order solutions. This set of equations has been solved approximately by a singular perturbation method for a linear temperature distribution on the top and bottom boundaries by Quon (1980), and for a sinusoidal temperature distribution on the bottom by Daniels (1976). The results are as follows: the heat transfer is by conduction and the temperature field generates an azimuthal velocity because of the thermal-wind balance. Along the top and bottom boundaries are Ekman layers and along the sidewalls are $E^{\frac{1}{3}}$ Stewartson–Proudman layers. Because of the insulated boundaries, the azimuthal velocity generated by the thermal wind balance satisfies the boundary conditions on the sidewalls automatically, i.e. $v = 0$ at $x = 0, 1$. Consequently, in the $E^{\frac{1}{3}}$ layers Ψ only acquires an $O(E^{\frac{1}{3}})$ strength which is insufficient to support the Ekman transport, which is $O(E^{\frac{1}{2}})$. The communication between the upper and lower Ekman layer is forced through the interior by Ekman suction (for details see Daniels 1976; Quon 1980). Note that it is not necessary to introduce an $E^{\frac{1}{4}}$ layer for this problem because

$$\int_0^1 v(x, z)\,\mathrm{d}z = 0 \quad \text{at } x = 0, 1$$

(Hunter 1967; Daniels 1976).

As heating increases, i.e. as β increases from infinitesimal to some larger value, the linearized advective term becomes important in (4.3), i.e. with T replaced by T_0, the conduction temperature, on the left-hand side. We can eliminate T and v in (4.1)–(4.3) to form a side-boundary-layer equation:

$$\Psi_{\xi\xi\xi} + \sigma\beta E^{-\frac{1}{3}} T_{0z}\,\Psi_{\xi\xi} + \Psi_{zz} = 0, \tag{4.4a}$$

where $\xi = E^{-\frac{1}{3}}x$ is the stretched coordinate, $E^{\frac{1}{3}}$ being the boundary lengthscale, and $\partial T_0/\partial z$ the vertical temperature gradient on the vertical wall (see D & S).

If $\partial T_0/\partial z$ is zero, i.e. if the fluid is homogeneous (Stewartson 1957), or if the isotherms are nearly vertical on the sidewalls, such as in the conventional rotating

annulus problem which has the sidewall temperature kept constant (Robinson 1959; Hunter 1967), or, if β is infinitesimal so that the second term can be neglected as in Daniels (1976) and Quon (1980), (4.4a) represents the classical $E^{\frac{1}{3}}$ Stewartson–Proudman layer. If $\partial T_0/\partial z$ is positive, the solution for (4.4a) is still the Stewartson–Proudman layer which decays rapidly with distance from the sidewall. Physically, a positive $\partial T_0/\partial z$ means a gravitationally stable thermal stratification which damps any vertical motion. The crux of the problem lies in the fact that in the warm side of fluid cavity, $\partial T_0/\partial z$ is negative, and hence thermally unstable. D & S have dealt with this particular situation very thoroughly. We shall summarize some of their results so that we can on the one hand interpret the numerical solutions more readily, and on the other hand identify and assess the transient and nonlinear phenomena that these authors had not been able to include in their linear and weakly nonlinear theories.

(i) If we define $\lambda = \sigma\beta E^{-\frac{2}{3}}$ and set $\partial T_0/\partial z = -C$, C being a positive constant, then (4.4a) becomes

$$\Psi_{\theta\xi} - \lambda C \Psi_{\xi\xi} + \Psi_{zz} = 0. \tag{4.4b}$$

Recall from (2.8b) that an internal Rayleigh number can be defined as

$$Ra_{\mathrm{i}} = \sigma\beta E^{-2} \left| \frac{\partial T_0}{\partial z} \right| l^4.$$

If we let $|\partial T_0/\partial z| = C$, and $l = E^{\frac{1}{3}}$, then

$$Ra_{\mathrm{i}} = \sigma\beta E^{-2} C E^{\frac{4}{3}} = \sigma\beta E^{-\frac{2}{3}} C = \lambda C.$$

Therefore λC in (4.4b) is the internal Rayleigh number Ra_{i}. D & S found the critical Rayleigh number for a vertical wavenumber n when C is assumed to be a constant:

$$Ra_{\mathrm{c}}(n) = 3 \times 4^{\frac{1}{3}} (n\pi)^{\frac{4}{3}}, \quad n = 1, 2, 3, \ldots. \tag{4.5}$$

If $Ra_{\mathrm{i}} < Ra_{\mathrm{c}}(1)$, the solution decays into the interior. However, if $Ra_{\mathrm{i}} > Ra_{\mathrm{c}}(1)$, the solution becomes spatially oscillatory for large ξ, i.e. in the interior of the fluid cavity, and the boundary layer approach is no longer valid.

(ii) Assuming $\partial T_0/\partial z = -C(x)$, whose absolute magnitude decreases as x approaches $\frac{1}{2}$ from the sidewall so as to reflect the structure of the boundary temperature ($T = \frac{1}{2}\cos nx$), D & S analysed (4.1)–(4.3) by series expansion over the whole cavity (*vs.* boundary-layer analysis of (4.4b) as given above). Instead of (4.5), they found the critical Rayleigh number for a vertical wavenumber n to be

$$Ra_{\mathrm{c}}(n) = 8.6956\, n^{\frac{4}{3}} Ta^{\frac{2}{3}}, \quad n = 1, 2, 3\ldots, \tag{4.6}$$

where $Ta = E^{-2}$ is the Taylor number (note that this $Ra_{\mathrm{c}}(n)$ is essentially the same as that given in (4.5) except that here it is based on the lengthscale L instead of $(2E)^{\frac{1}{3}} L$). If $Ra_{\mathrm{i}} = \lambda C(x)$ is greater than $Ra_{\mathrm{c}}(n)$, the solutions are oscillatory in the form of cells with a vertical wave number n, and of width $O(E^{\frac{1}{3}})$. Since $C(x)$ is assumed to decrease with distance from the sidewall, cellular motion will cease to exist where Ra_{i} becomes less than critical. $C(x)$ therefore acts as a filter for the vertical wavenumber n. Cells with the smallest n penetrate furthest into the interior, because $Ra_{\mathrm{c}}(n)$ decreases with $n^{\frac{4}{3}}$ and Ra_{i} decreases with $C(x)$, as x increases. It is interesting to note that, as pointed out by D & S, $Ra_{\mathrm{c}}(1)$ is the same as that for Bénard instability in a rotating viscous fluid derived by Chandrasekhar (1961, p. 95) as $Ta \to \infty$, e.g. for $Ta = 10^{13}$, $Ra_{\mathrm{c}}(1) = 4.038 \times 10^9$ and that according to Chandrasekhar is 4.037×10^9.

(iii) If $\partial T_0/\partial z = -C(x,z)$, i.e. the temperature gradient being allowed to vary with both x and z, the task of finding a critical Rayleigh number is considerably more difficult. D & S had to evaluate eigenvalues numerically in order to find the corresponding critical Rayleigh numbers. The general concept for (ii) still holds. However, the linear theory yields results whose denominator becomes zero for certain discrete frequencies. D & S identify these as resonant frequencies of the cavity.

(iv) D & S also developed a weakly nonlinear theory that includes the temporal and nonlinear terms in the momentum equations. The resonance in the linear theory was removed by a nonlinear effect. The weakly nonlinear theory was then carried over for a supercritical Rayleigh number $O(E^{-1})$ beyond $Ra_c(n)$ in (4.6). The stability of the flow at supercritical Rayleigh number was investigated.

Though D & S provide a great deal of insight on the flows in the system as a whole, the solutions are far too complex for detailed comparison with numerical or experimental results. These analyses themselves also raise a variety of questions. Perhaps the most important ones are the questions of possible bifurcation of the solutions, and the nature of their instability. As the authors have noted, it is not clear after crossing over the critical Rayleigh number to a supercritical value whether the instability is an exchange instability in the sense that a new state will emerge, or catastrophic instability from which the ensuing motion is turbulent. Furthermore, would the solutions bifurcate in parameter space and/or in time? What are the truly nonlinear states? What are the transient states? Do steady states exist for certain parameter range?

Having only a limited number of solutions to discuss below, we shall only attempt to provide partial answers to some of these questions. For example, organized flows (rather than turbulent flows) do exist in the highly nonlinear regime. The transition from initially unstable states to final steady states seems to be orderly. The serious question of the effect of the third space dimension on the flows cannot be dealt with here.

In the rest of the paper, we shall present the results in two parts: §§5–8 for steady and quasi-steady-states, which includes an analysis on a viscous non-diffusive boundary layer in the Appendix; and §9 for transient states, which includes the onset of instabilities.

5. Steady and quasi-steady states

The contour maps of the steady and quasi-steady states of all five cases are grouped in figure 3 for ease of comparison. The top row depicts the isotherms, the middle row the stream functions, and the bottom row, the zonal (azimuthal) velocities. Starting from the column at the extreme left, the maps become less symmetric about the vertical centreline as one proceeds towards the right. The asymmetry of the contour lines increases with the severity of the advective effect on temperature distributions as β becomes larger. However, in spite of the apparent differences between the different cases, one can make certain common dynamical inferences from them.

When E is small, the viscous terms in (2.1)–(2.3) are negligible in the interior region where geostrophy holds at steady state (this is true for all the five sets of parameters under study here). Infinitesimal E would confine the Ekman boundary layer, being $O(E^{\frac{1}{2}})$ in thickness, to very small regions near the upper and lower boundaries. In the interior, geostrophy implies a thermal wind balance, i.e. $\partial v/\partial z = \beta\,\partial T/\partial x$, and $\partial \Psi/\partial z = 0$. Consequently, if there is any meridional flow in the interior of the fluid at all, i.e. $\Psi = \Psi(x) \neq$ constant, it must arise from Ekman suction. The interior

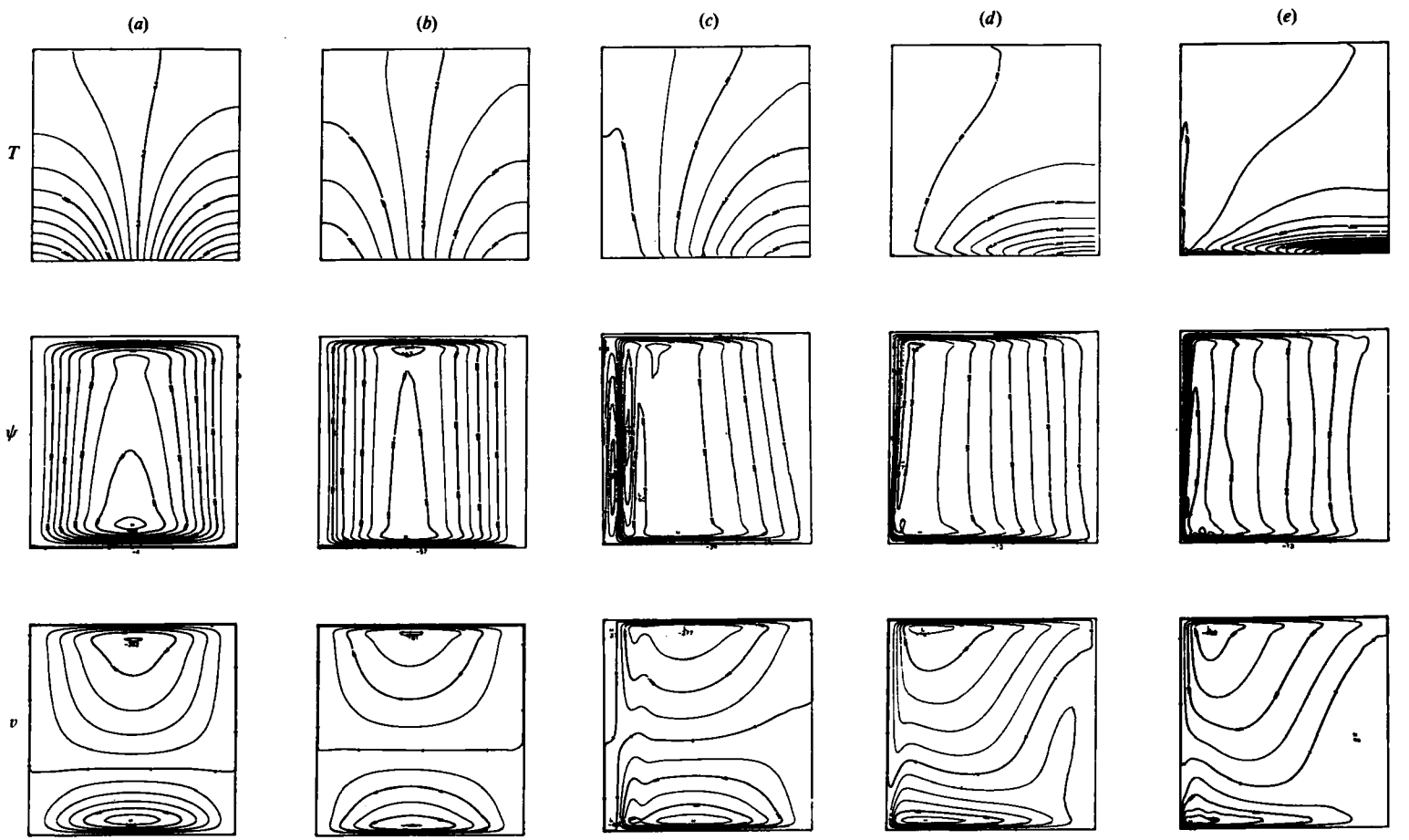

FIGURE 3. Contour maps of temperature, stream functions and azimuthal velocities of five cases: (*a*) case 1–(*e*) case 5. Note that the contour intervals of the temperature for case 1 and case 5 are 0.05 and those of the other cases are 0.10. The minima of Ψ and maxima and minima of v are given in table 1.

meridional flow would be $O(E^{\frac{1}{2}})$ smaller than the Ekman layer velocities; the zonal velocity in the interior is characterized by a vertical shear whose strength is proportional to the local horizontal temperature gradient. The structure of the side boundary layers, however, varies with β. In order to discuss the flow fields and temperature distribution in greater detail, we shall divide the five cases into three groups: group A consists of cases 1 and 2, which are essentially linear; group B contains case 3, which is weakly nonlinear; and cases 4 and 5 constitute group C, which is highly nonlinear.

A *Linear heat transfer, case 1, $\beta = 0.001$, and case 2, $\beta = 0.005$*

The stream function Ψ and zonal velocity v for both cases 1 and 2 are almost symmetric about the vertical centreline of the cavity, while the temperature distributions, which are the driving force of the flows, are nearly antisymmetric for both cases (see figure 3*a*, *b*). The slight asymmetry in the isotherms indicates that thermal convection begins to play a minor role in heat transfer in the interior of these two systems. (Note that the contour intervals of temperature for case 1 and case 5 are 0.05 instead of 0.10 as in all the other cases.) On the whole, conduction is the dominant mechanism of heat transfer for both cases. Hence the steady states of both these cases can be reasonably well described by the linear theory. In the interior, the vertical shear in the zonal velocity, being controlled by the horizontal temperature gradient, is stronger at the bottom than at the top. The Ekman layers bring both the meridional and zonal flows in the interior down to zero to meet the boundary conditions on the top and bottom boundaries. Note that the Ekman-layer thickness of case 1 should be exactly twice that of case 2 because the Ekman number is exactly 4 times as large. The side layers are passive for infinitesimal values of β. The meridional circulation essentially consists of a single cell, upwelling in the left (warm) half and downwelling in the right (cold) half of the cavity. There is no cross-cavity flow in the interior, i.e. streamlines are almost vertical. As shown in table 1, the zonal velocity v maximum (near the bottom) is higher than the absolute v minimum by 20 %, although the linear theory predicts equal strength. We must, however, keep in mind that the theory is for $\sigma\beta = 0$. In spite of the similarity in the final steady states, case 1 and case 2 differ markedly in their transient states, as we shall describe later.

B *Weakly nonlinear heat transfer, case 3, $\beta = 0.02$*

Of the five cases studied here, only case 3 can sustain cellular motion near the warm vertical boundary after the computation has reached steady state. An inspection of figure 3(*c*) indicates that the cellular circulation occupies a region that is thermally unstable, approximately $\frac{1}{5}$ of the total cavity in the extreme left (also shown in figure 5). The vertical wavenumber is unity and cell width is almost exactly $(2E)^{\frac{1}{3}}$, (or $E^{\frac{1}{3}}$ as defined by D & S). According to the linear theory, boundary cells exist only if the internal Rayleigh number is greater than $Ra_c(n) = 8.6956 \times (n\pi)^{\frac{4}{3}}Ta^{\frac{2}{3}} = 1.091 \times 10^6$ for $n = 1$. The best numerical estimate of the vertical temperature gradient at the wall is $\Delta T/\Delta z = -0.103$ at $z = 0.5$ (figure 4). Using this non-dimensional temperature gradient, the local Rayleigh number becomes 9.156×10^5 which is close to but still less than the theoretical critical Rayleigh number. However, as we can see from figure 4 the vertical temperature gradient is a variable function of z. For case 3, the extreme value for $\Delta T/\Delta z$ is about -0.50. We can therefore use D & S's theory only as a guide. The exact criterion for the instability that creates the cells cannot be ascertained from the numerical solutions given here. In the rest of the cavity, the flows are geostrophically balanced. The positive isotherms have

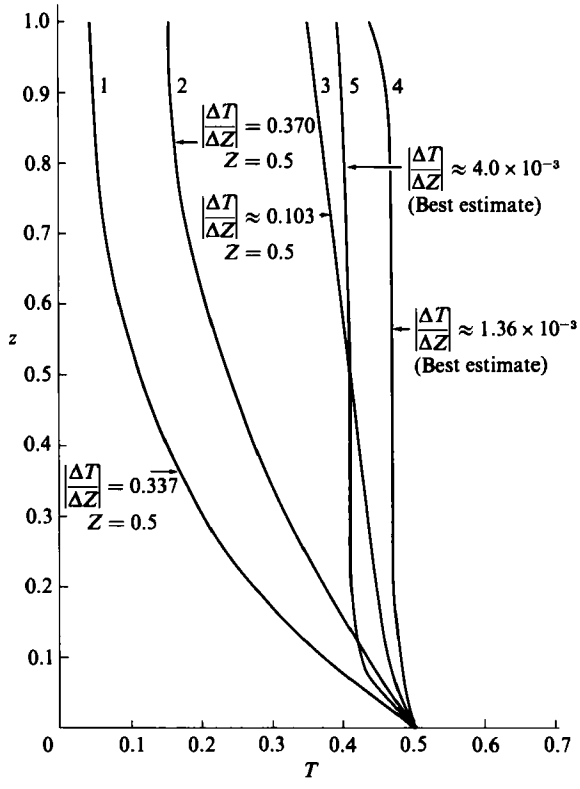

FIGURE 4. Vertical distribution of temperature on the wall at $x = 0$ for the five cases.

been advected much further to the right and the negative isotherms much further down towards the bottom boundary than case 2. Near the vertical boundary on the left, the upwelling and downwelling of the cellular motion have visibly modified the isotherms (figure 3*c*). Advection and diffusion are very delicately balanced to maintain a negative vertical temperature gradient large enough to sustain the cells. While the thermal wind (azimuthal velocity) has changed in accord with the temperature distribution in the interior, the zonal velocity has also responded to the cellular motion in the boundary region at the left as shown in figure 3(*c*).

Figure 5 shows a comparison of the horizontal distribution of various fields for case 1 and case 3 at two values of z. Specifically we see that: (i) by comparing figures 5(*a* and *b*), the vertical distributions of v and T are very similar in regions away from the left-hand side boundary at all levels; (ii) the horizontal distribution of T shows that while $T(x)$ for case 1 changes sign at $x = \frac{1}{2}$ at both heights, $T(x)$ for the upper level of case 3 remains positive for all x. This indicates that for case 3, the fluid in the whole cavity has warmed up considerably in comparison with case 1. However, note that the functional shapes of $T(x)$ remain very similar for both cases. Since $\partial v/\partial z = \beta \partial T/\partial x$ is the interior balance, some similarity is expected of the vertical shear of the zonal velocity in the interior. (iii) $v(x)$ at both heights appears to be very different near the left boundary for the two cases. The oscillatory parts are in response to the convection cells. They asymptotically match onto the interior solution. (iv) $w(x)$ are very different between the two cases: the $w(x)$ for case 1 is antisymmetric about $x = \frac{1}{2}$. For case 3, over the right-hand $\frac{4}{5}$ of the cavity down-

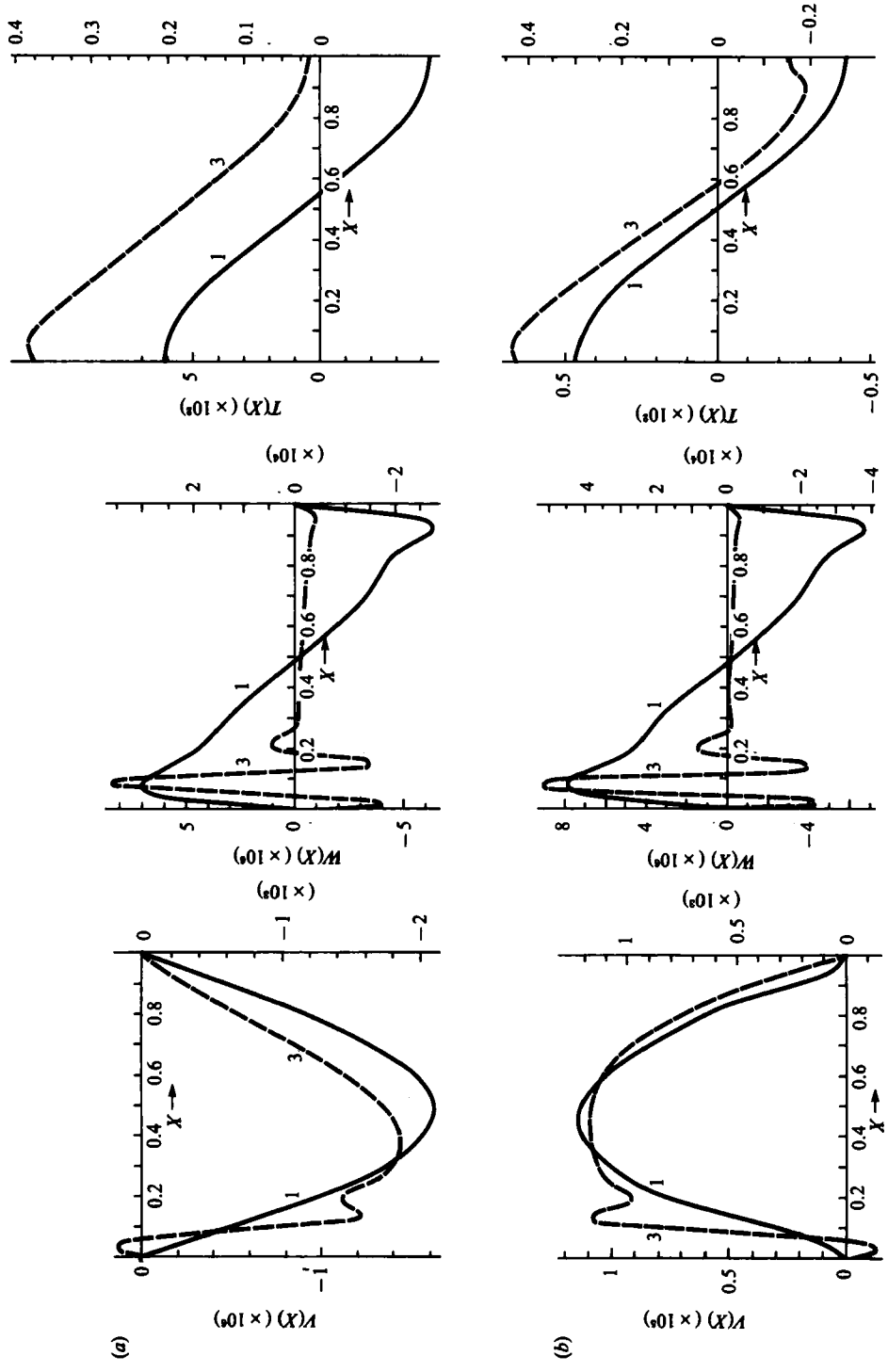

FIGURE 5. w, v and T as functions of x for case 1 and case 3 at (*a*) $z = 0.742$, (*b*) $z = 0.258$. The right-hand-side scales are for case 3 (dashed lines).

welling is apparent, and over this region $w(x)$ is almost linear in x. The dominant feature of the vertical motion is the cellular circulation next to the left-hand boundary which is an order of magnitude larger than the downdraught in the interior. The three cells are almost equal in width, $\approx (2E)^{\frac{1}{3}} \approx 6.7 \times 10^{-2}$. The edge of the outer cell is at $x \approx 3 \times (2E)^{\frac{1}{3}} \approx \frac{1}{5}$ of the cavity width. It is clear by comparing the isotherms of case 3 and case 1 (figure 3) that we cannot consider the former as a perturbed state of the latter as the linear theory would require. Obviously, advection plays a very important role in the heat transfer of case 3.

C *Nonlinear heat transfer, case 4, $\beta = 0.20$ and case 5, $\beta = 1.0$*

These two cases are highly nonlinear. The meridional flows have reverted back to one-cell circulations as represented by Ψ in figures 3(*d* and *e*). For both cases downwelling spans the entire interior except for a narrow region next to the left-hand side boundary where a very strong boundary jet carries the entire upward mass transport of the cavity and where the fluid is almost isothermal. This boundary layer is nonlinear. We shall give a more detailed discussion in §7. Over the entire interior, strong downwelling packs isotherms down to the bottom boundary. The upper part of the cavity is almost isothermal. Note that the meridional circulation is reminiscent of Stommel's conjecture of the small sinking region of the oceans while the temperature distribution reminds one of the conventional thermocline theory (Needler 1967). Stern (1975) had discussed the hydrostatic equivalent of this problem in an attempt to elucidate the oceanic thermocline problem.

Although the steady states of both cases appear to be quite similar, case 5 in fact is only quasi-steady. The lower left corner seems to remain active and thermally unstable. Inertial gravity waves emanate from this corner and propagate away and upward along the isotherms. Oscillations of low frequencies (possibly eigenfrequencies of the cavity) are excited and then get absorbed in the stable region. As viewed from a computer movie, the streamlines appear to vibrate like strings fixed at both ends at some internal characteristic frequency. No steady state is attainable for case 5 although case 4 has reached one. Figure 3(*e*) represents only a snapshot of the flow in the interior. Further discussion on the time-dependent motion is given in §9.

6. Comparison with an experiment

Hignett *et al.* (1981) reported on a series of laboratory experiments of this problem. Although they have not reported on the transient flows, they have made substantial measurements of the temperature fields, and deduced interior flows with the help of some visual estimates of flow speeds at discrete locations in the fluid. Of these experiments one is particularly interesting to us because its parameters are almost the same as those of case 5: aspect ratio of container ≈ 1, $\sigma = 6.75$ (*vs.* 10), $E = 1.55 \times 10^{-4}$ (*vs.* 1.5×10^{-4}), and $Ra = 2.38 \times 10^8$ (*vs.* 4.44×10^8). By $Ra = \sigma\beta E^{-2}$, the thermal Rossby number for the laboratory experiment is $\beta = Ra\, E^2 \sigma^{-1} = 0.801$ (*vs.* 1.0 for case 5). The experiment also showed that the flows are axisymmetric for this set of parameters. This last attribute is particularly important because the computations are two-dimensional. In addition to these differences the laboratory experiment was carried out in an annulus with gap-to-inner-radius ratio $= O(1)$ while that for the numerical experiment is zero, i.e. a narrow-gap approximation has been used. Furthermore, the imposed temperature at the bottom is sinusoidal for the numerical experiment, while that for the laboratory experiment is proportional to $\ln r$, because the temperature is generated by conduc-

tion in the radial direction. In spite of these differences the distributions of isotherms are very similar. In the numerical experiment, the bulk of the interior is above $0.80\Delta T$ (non-dimensional $T > 0.30$) which is essentially what the laboratory results are. The vertical profiles of the temperature and horizontal velocities in the buoyant Ekman layer are very similar to those in the laboratory experiment (see figure 6*a* below).

7. A viscous, non-diffusive boundary layer

In Table 2(*a*) we show the balance of terms in all the equations for the point at $x = 0.0261$ and $z = 0.742$, which is well within the $E^{\frac{1}{3}}$ layer (cf. $E^{\frac{1}{3}} = 0.0532$). The lowest-order balances in the u-equation in row 1 and the w-equation in row 3 are essentially geostrophic, ($p_x = v + \Delta_1$), and hydrostatic ($p_z = \beta T + \Delta_2$), where Δ_1 and Δ_2 are higher-order corrections. Furthermore, $-\Delta_2 = Ew_{xx}$ has been established in the w-equation. This balance gives a steady vertical velocity in the boundary layer. The balance between the advective terms in the T-equation in row 4 is almost exact. Hence the diffusion of heat is unimportant at steady state in the vertical boundary layer! In the u-equation, Δ_1 is an order-of-magnitude higher than Eu_{xx}. The terms in the v-equation in row 2 are also grossly unbalanced. We are forced to conclude that the u- and v-equations have not yet reached steady state. This unsteadiness will be further discussed in §9. It is nevertheless apparent that we can assume the following approximate balances for steady state:

$$(p_x - v) - \Delta_1 = Eu_{xx},$$
$$u = Ev_{xx} + \text{nonlinearity},$$
$$(p_z - \beta T) - \Delta_2 = Ew_{xx},$$
$$(uT)_x + (\omega T)_z = 0.$$

Based upon these balances, it will be useful to postulate, even if only crudely, an even simpler approximate dynamical balance to see whether it is possible to construct a stable and steady vertical boundary layer that reflects the numerical solution shown in figure 3(*d*, *e*).

We shall start with the above equations without nonlinearity in the second equation. The neglect of the inertial terms in all the momentum equations and the diffusive term in the T-equation can be justified on the basis of large σ. Thus the fluid is considered to be viscous but non-diffusive in the boundary region. Combining the above equations, and replacing u by $-\Psi_z$ and w by Ψ_x we have

$$\frac{\partial v}{\partial z} = \frac{\partial T}{\partial x} + E\nabla^4\Psi, \tag{7.1a}$$

$$-\frac{\partial \Psi}{\partial z} = E\nabla^2 v, \tag{7.1b}$$

$$-\frac{\partial \Psi}{\partial z}\frac{\partial T}{\partial x} + \frac{\partial \Psi}{\partial x}\frac{\partial T}{\partial z} = 0. \tag{7.1c}$$

The boundary conditions are

$$\left.\begin{aligned} \Psi = \frac{\partial \Psi}{\partial x} = 0 \quad v = 0, \quad \text{at } x = 0, \\ \Psi \to \Psi^{\mathrm{I}}(0), \quad v \to v^{\mathrm{I}}(0), \quad \text{in the interior,} \end{aligned}\right\} \tag{7.2}$$

and

(*a*)

$(u^2)_x$	+	$(wu)_x$	−	v	=	$-p_x$	+	EU_{xx}	+	EU_{zz}	+	$u\nabla\cdot v$
3.871(−6)		−6.349(−6)		−1.443(−2)		−1.461(−2)		−1.733(−5)		−5.496(−7)		−1.766(−8)
$(uv)_x$	+	$(wv)_z$	+	u	=	Ev_{xx}	+	EV_{zz}	+	$v\nabla\cdot v$		
−1.526(−4)		6.985(−5)		2.744(−4)		5.584(−4)		4.991(−6)		3.905(−7)		
$(uw)_x$	+	$(w^2)_z$	=	$-p_z$	+	βT	+	EW_{xx}	+	EW_{zz}	+	$w\nabla\cdot v$
3.415(−5)		−5.616(−6)		0.40729		0.40764		−3.681(−4)		3.705(−6)		−2.196(−7)
$(uT)_x$	+	$(wT)_z$	=	$E/\sigma T_{xx}$	+	$E/\sigma T_{zz}$	+	$T\nabla\cdot v$				
1.411(−3)		−1.412(−3)		−6.724(−6)		−1.860(−7)		−2.101(−5)				

(*b*)

$(u^2)_x$	+	$(wu)_x$	−	v	=	$-p_x$	+	EU_{xx}	+	EU_{zz}	+	$u\nabla\cdot v$
−3.667(−4)		−5.932(−4)		2.254(−2)		3.864(−2)		4.632(−6)		−1.606(−2)		−5.696(−6)
$(uv)_x$	+	$(wv)_z$	+	u	=	EV_{xx}	+	EV_{zz}	+	$v\nabla\cdot v$		
7.192(−4)		−8.430(−4)		−1.477(−2)		−1.841(−5)		−1.492(−2)		−1.124(−6)		
$(uw)_x$	+	$(w^2)_z$	=	$-p_z$	+	βT	+	EW_{xx}	+	EW_{zz}	+	$w\nabla\cdot v$
−1.231(−5)		−1.264(−5)		0.1743075		0.1746750		2.827(−5)		1.984(−4)		5.848(−7)
$(uT)_x$	+	$(wT)_z$	=	$E/\sigma T_{xx}$	+	$E/\sigma T_{zz}$	+	$T\nabla\cdot v$				
1.290(−2)		−3.114(−3)		7.672(−5)		9.323(−3)		−8.996(−6)				
$-v_z$	+	βT_x	=	EU_{zzz}								
1.264		−4.356(−1)		−1.744								

TABLE 2. (*a*) Balance of terms for case 5 at $x = 2.61 \times 10^{-2}, z = 0.742$. Note that the last terms are computational errors because $\nabla\cdot v$ is not zero owing to truncation error. The numbers in parentheses are exponents. (*b*) Balance of terms at $x = 0.2942, z = 1.24 \times 10^{-2}$.

where $\Psi^{\mathrm{I}}(0)$ and $v^{\mathrm{I}}(0)$ are the asymptotic values of Ψ and v, which are also the value of the interior solutions Ψ and v at $x = 0$. In the Appendix we show that the highly nonlinear regime can indeed admit a steady and stable boundary-layer solution.

8. The buoyant Ekman layer and the coefficients of heat transfer

For the highly nonlinear case 5, the upper part of the cavity is essentially isothermal (see figure 3*e*), and the dynamical balance there at steady state is basically the Ekman-layer balance. However, near the bottom boundary, the heat transfer is expected to be advective–diffusive, and the dynamical boundary layer to be a buoyant Ekman layer.

Table 2(*b*) shows the dynamical and thermal balances at the point $x = 0.2942$ and $z = 0.0124$, well within the Ekman layer (cf. $E^{\frac{1}{2}} = 0.0125$). Row 1 in table 2(*b*) shows that the balance in the u-equation comprises the Coriolis force, the horizontal pressure gradient, and vertical diffusion. Row 3 shows that the primary contribution to the pressure distribution is from the temperature variation through the hydrostatic balance. Combining the u- and w-equations by eliminating p, we obtain the equation in row 5 which shows the buoyancy term βT_x to be of comparable importance to the overall balance. The v-equation in row 2 and the combined equation in row 5 define a buoyant Ekman boundary layer as expected. Row 4 shows that the heat transfer is carried out by horizontal advection and vertical diffusion, with a substantial contribution from vertical advection. Therefore in the lower boundary region, the approximate description of the boundary layer is given by

$$-v_z = -\beta T_x + E u_{zzz}, \tag{8.1}$$

$$u = E v_{zz}, \tag{8.2}$$

$$(uT)_x + (wT)_z = \frac{E}{\sigma} T_{zz}. \tag{8.3}$$

This set of equations is quite similar to (7.1), except that heat diffusion is important here. This additional term makes it much more difficult to find an approximate analytical solution.

Figure 6(*a*) shows the vertical profiles of the numerical solutions u, v and T in the buoyant Ekman layer at $x = 0.1, 0.5$, and 0.9 (note the different scales of the different graphs). If we take the first zero of u inside the fluid as a measure of its thickness, this boundary layer is uniformly thick over the entire span of x. The v-profiles vary substantially at the three positions of x because the asymptotic conditions are different (v^{I} in the interior). The temperature profiles are even more different at the three values of x because both the boundary conditions at $z = 0$ and the asymptotic conditions are different at different values of x.

Figure 6(*b*) shows the plot of the vertical temperature gradients at $z = 0$ as a function of the horizontal coordinate. The oscillatory parts reflect the influence of the cellular motion. The curve marked case 0 is a plot of the vertical temperature gradient of the theoretical conduction solution at $z = 0$. The integral

$$\int_{x=0}^{1} \frac{\partial T}{\partial z} \mathrm{d}x$$

vanishes because both the heat input and output are through the bottom boundary. For the numerical solutions, this integral never completely vanishes. For case 1, the

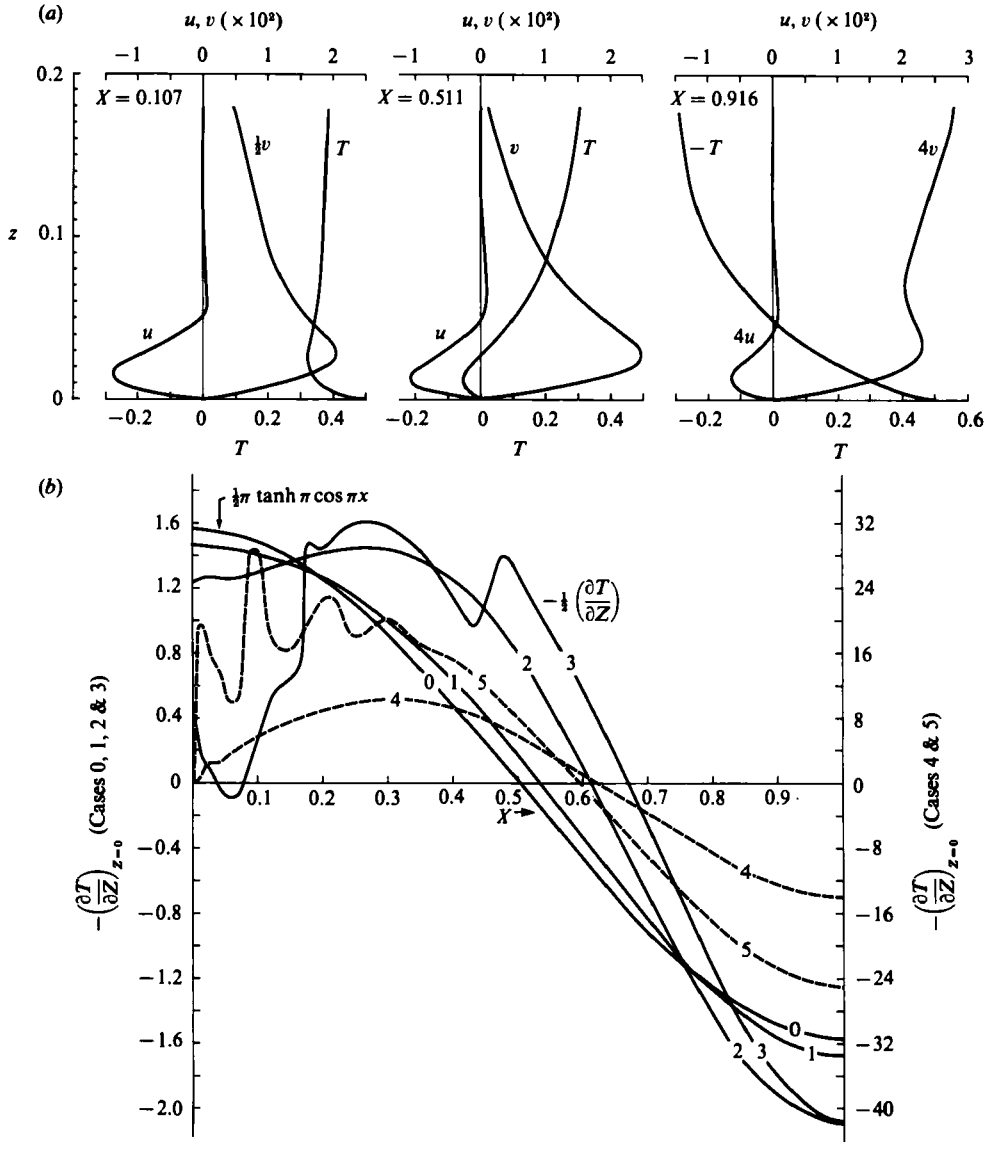

FIGURE 6. (*a*) Vertical profiles of u, v and T of case 5 in the bottom boundary layer at three horizontal positions. Note the change of scales. (*b*) Vertical temperature gradients of all five cases at $z = 0$. Note the change of scales. The right-hand-side scale is for cases 4 and 5 (dashed lines).

finite-difference summation of the temperature gradient at the bottom is close to zero. For the other cases, the differences between the positive and negative parts range from 2% (case 1) to 15% (case 5). The reasons for these discrepancies are twofold. (*a*) The finite-difference summations are in error because the variable grids in the horizontal direction makes it difficult to represent the integral accurately by simple summations (more accurate results are possible, e.g. by fitting the curves in figure 6(*b*) to Chebyshev polynomials, and then computing the integrals from these polynomials). (*b*) The positive part of this integral is always larger than the negative part, i.e. the heat input is always larger than the heat output. This, together with the

Case	1	2	3	4	5
$\overline{Nu}$	1.06	1.32	2.37	7.91	16.58

TABLE 3. The averaged Nusselt numbers

integral of the temperature variant (not shown), which are still increasing slowly with time, indicate that the systems have not yet reached thermal equilibrium completely. The final stages of development are largely by diffusion, and are very slow processes.

To compute the coefficients of heat transfer, or the Nusselt numbers, we have taken the positive (or negative) part of the integral for case 0 as the basic conductive heat transfer, and designated it by I_0. Next we computed the average of the absolute values of the positive and negative parts of the five integrals and designate them by $I_j, j = 1$–5 representing the 5 cases. The ratios $I_j/I_0 = Nu_j$ are the Nusselt numbers, which are listed in table 3. Case 5, which is a very advective case, has $Nu_5 = 16.58$. This indicates that the heat transfer rate of case 5 is 16 times that of the conduction state. Note that because of 15 % maximum error discussed above, there is a maximum 7.5 % uncertainty in the mean Nusselt numbers.

9. The transient states

The transient states of all five cases provide a substantial amount of information that can lead to a better understanding of the steady states. The transients are sometimes extremely volatile, and, as expected, are quite different for the various ranges of the thermal Rossby number. For clarity, we shall first discuss them separately and then compare them. All computations start with solid-body rotation (i.e. zero velocity relative to the rotating frame of reference) and at reference temperature (i.e. $T = 0$). Heat conduction initially sets up similar temperature profiles adjacent to the bottom boundary for all cases. However, how fast the velocity fields develop and how the instabilities come about depend on β.

Case 1

The transient state of case 1 is very benign (not shown). Since the flows hardly affect the temperature field even at steady state, we shall discuss the temperature and flow fields independently although they always develop concurrently. As the isotherms advance into the interior from the bottom boundary by conduction, a one-cell circulation develops. At first, this cell adheres to the bottom boundary and is dominated by a buoyant Ekman layer because heat has not yet had time to diffuse into the interior. Gradually the cell spreads into the interior with the isotherms. As the horizontal temperature gradient becomes stronger in the interior, the thermal wind develops while the Ekman layers strengthen to help the interior flow fields to meet the upper and lower boundary conditions. Although dynamically the effects of both buoyancy and rotation are experienced by the fluid immediately, the thermal effect has to take a slight lead in order to initiate the motion. An important observation for case 1 is the following. Although one half of the cavity is gravitationally unstable throughout the experiment, at no time has the Rayleigh

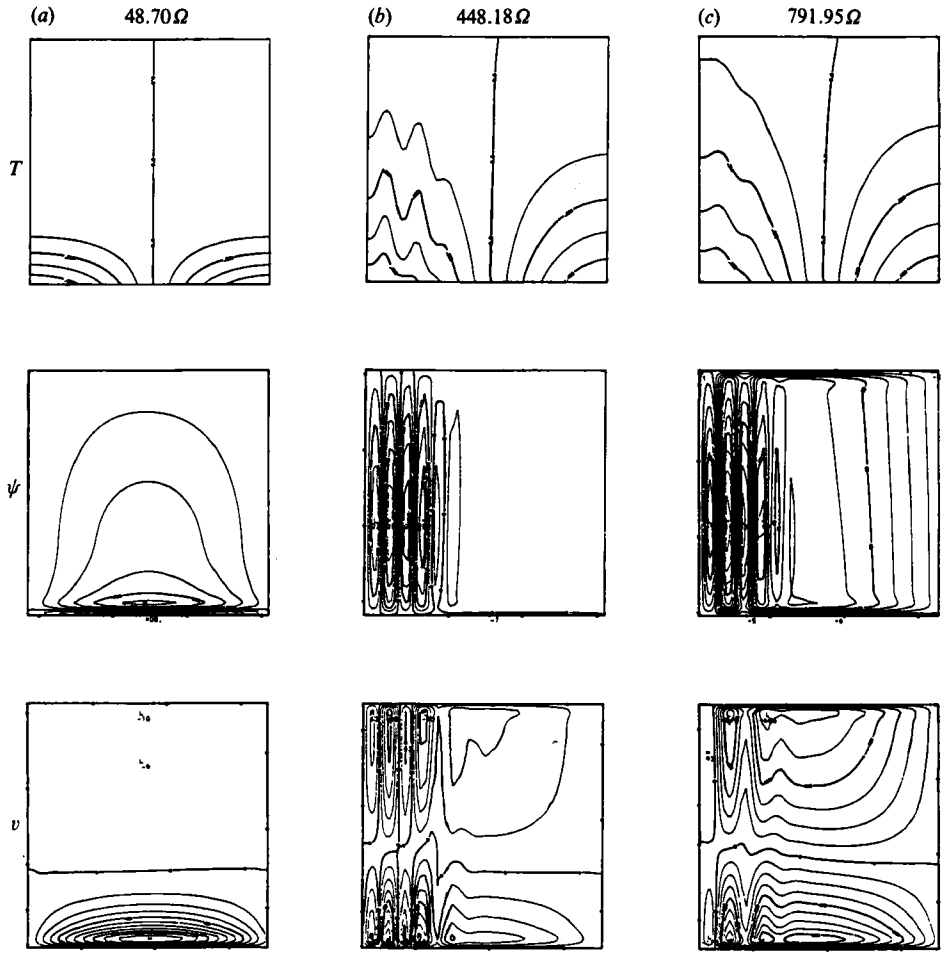

FIGURE 7. Time-dependent development of case 2. Time in rotations.

number reached the critical value, and hence no cellular instability ever occurs during the experiment.

Case 2

Although the steady states of case 2 are very similar to those of case 1, the transient states are markedly different. As table 1 shows, the external Rayleigh number of case 2 (in fact of all cases except case 1) is larger than the critical Rayleigh number $Ra_c(1)$, and hence case 2 is expected to undergo cellular instability. However, we must recall that the total temperature difference, ΔT is used to define the external Rayleigh number while at no time is the temperature between the top and bottom boundary larger than $\frac{1}{2}\Delta T$. Therefore the effective Rayleigh number is halved, or $Ra = 1.110 \times 10^6$ which is only slightly larger than $Ra_c(1) = 1.091 \times 10^6$. Because the vertical temperature distribution is not linear and because advection, though slight, has further reduced the total vertical temperature difference, the effective Rayleigh number at steady state is in fact less than critical.

The transient states, however, do exhibit instability. Figure 7(*a*) shows that the

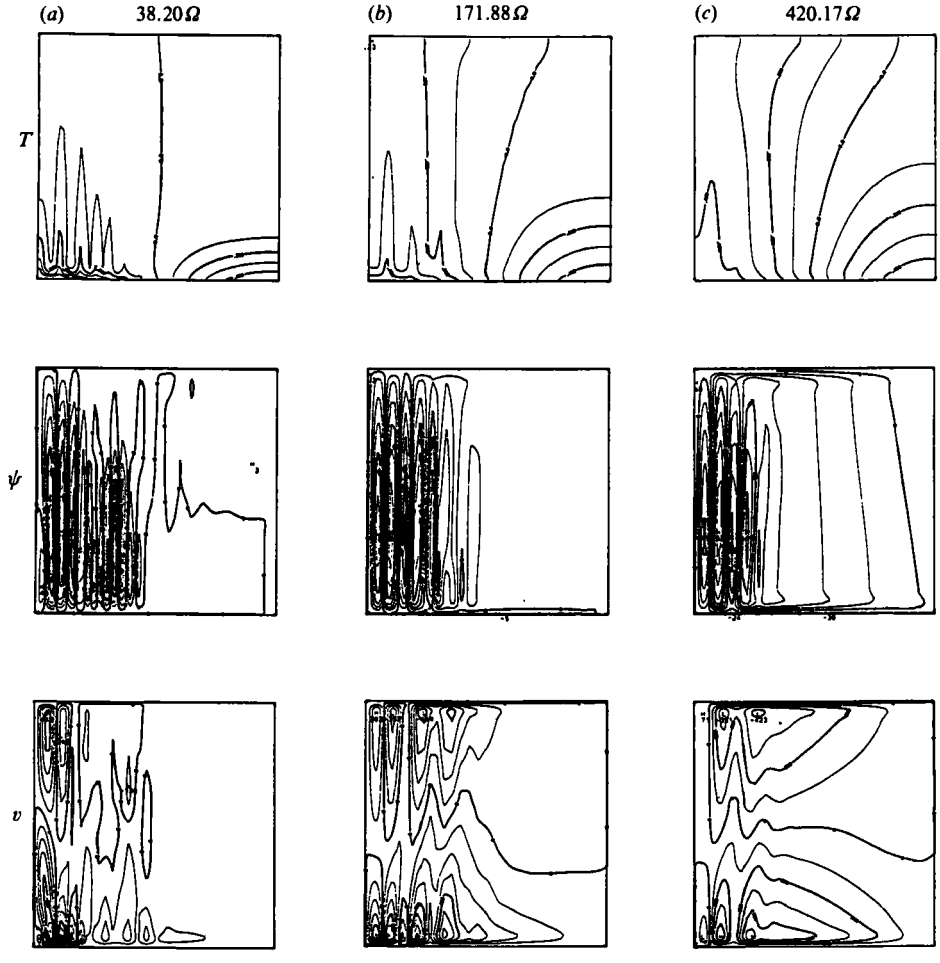

FIGURE 8. Time-dependent development of case 3. Time in rotations.

flows are not yet unstable at rotation 48.70. However, approximately 146 rotations after the start of heating (not shown, 1 rotation = 4π dimensionless time) instability sets in; 76 rotations later, four cells have fully developed. At the peak of total integrated kinetic energy (not shown), approximately 438 rotations after the start of heating, there are five discernible tall cells of width = $O(2E)^{\frac{1}{3}}$ as shown in figure 7 (*b*). They produce large-amplitude waves on the isotherms in the unstable half of the cavity as shown in the T-frames of figure 7 (*b*, *c*), the temperature frames. The motion in the right-hand half of the cavity is negligibly small, and the temperature maintains its conduction profile. Although cellular advection becomes visibly important in the heat transfer in the left half of the cavity, the perturbed isotherms continue to move upward by conduction. The vertical temperature gradient thus weakens as the isotherms spread. In the meantime, starting from the interior of the cavity all the cells are diminishing in strength and are quickly dissolving themselves, starting from the outer cells. Eventually the vertical temperature gradient become too small to sustain any cellular motion. The cells disappear altogether, and a one-cell steady state is then enhanced. The final steady state becomes very similar to that of case 1

as shown in figure 3(*b*). The spatial oscillations persist for more than 1050 rotations before they completely disappear.

Recalling that this case has only an infinitesimal value for $\sigma\beta (= 5 \times 10^{-2})$, we recognize that the D & S theory should be appropriate. The cellular instabilities of this case develop only after the side boundary layers have been well established. As we shall see later, when β is sufficiently large instability can occur much earlier. The special characteristics of this transient state are the following: (*a*) instability sets in only after the side boundary layers have developed and only after the rotation has established its effect; (*b*) over a duration of 1050 rotations five cells have developed and decayed; (*c*) the steady states revert to a one-cell circulation similar to those of case 1. An in-depth discussion of the instability and temporal development of this case is given in Quon (1986).

Case 3

As pointed out above, this is the only case that maintains permanent steady cells. The transient state undergoes cellular convection very early on. The best estimate shows that cellular motion starts about 9.5 rotations after the heating start.

Unlike case 2, whose cell developments are very slow, and whose cellular motion does not affect the isotherms immediately, case 3 undergoes very rapid changes in all fields as soon as the cellular instability has taken place. Isotherms very rapidly acquire a spiky appearance in the unstable region due to advection by the cells as shown in figure 8(*a*). Initially very small cells, whose lengthscale is of the thickness of the thermal layer, form at the lower left corner, and spread horizontally to the right. Although they also penetrate upward, they have only one cell in the vertical. The cells become taller but remain thin. The cellular activities reach their maximum approximately at rotation 50, when there are six thin vertical cells reaching the top boundary, occupying almost the entire unstable half of the cavity, figure 8(*a*, *b*). At steady state, there are only three tall cells spanning over an area about $\frac{1}{5}$ the cavity as shown in figure 3(*c*). The outer cell is rather weak.

The main differences between the transient states of case 2 and 3 are in the development of the isotherms. For case 2, the cells only perturb the isotherms. The perturbations deform the isotherms in the unstable half of the cavity into configurations of vibrating strings. These perturbations are relatively small in comparison with the values of the isotherms themselves, figure 7(*b*). For case 3, however, the cellular motion has produced a finite-amplitude effect on the isotherms. Advection of the cells makes the isotherms spiky with their upward motion, and compresses the isotherms with their downward motion, figure 8(*b*, *c*), although at steady state diffusion has smoothed out the isotherms as shown in figure 3(*c*). The cells are basically the spatial oscillations postulated by D & S.

Case 4 and case 5

As described above, cases 1–3 essentially belong to the conductive regime. Their flows either undergo no instability as case 1, transient spatial oscillations as case 2, or permanent steady spatial oscillations as case 3. All these cases are within the parameter range considered by D & S. Their linear and weakly nonlinear theories can be applied to explain some of these flow phenomena to a greater or lesser extent.

Cases 4 and 5 are highly nonlinear. Their transient states go through two very distinct unstable stages before reaching steady state or quasi-steady state. Since the transient states of both cases are quite similar, we shall only describe those of case 5.

Before describing the two-dimensional transient flows, we shall first study

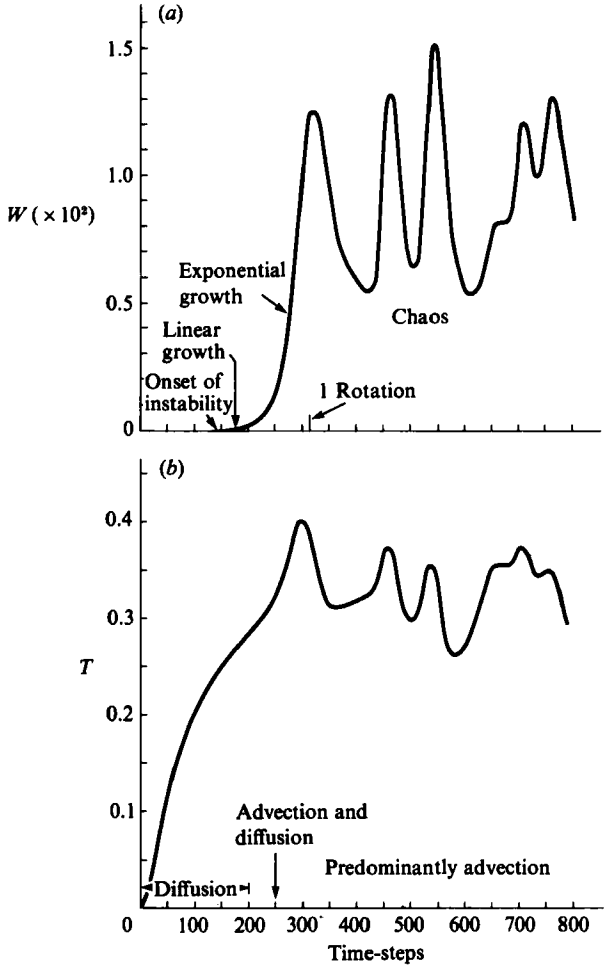

FIGURE 9. Time-dependent development of (*a*) w and (*b*) T of case 5 at $x = 1.434 \times 10^{-3}, z \approx 10^{-2}$. One time-step = 0.04 units of dimensionless time (1 rotation = 4π units of dimensionless time).

figure 9(*a* and *b*), which respectively are plots of the vertical velocity w and temperature T against time-steps of computation at $x = 1.434 \times 10^{-3}$, $z \approx 10^{-2}$, a point in the unstable corner. Figure 9(*a*) shows that up to time-step 150, about half a rotation after the start of the computation, the vertical velocity is infinitesimal. Between time-steps 150 and 200, the velocity grows linearly with time. This is the duration of linear instability. From time-step 200 onward, the velocity grows exponentially. Beyond time-step 300, the velocity becomes irregular.

Figure 9(*b*) shows a similar growth for the temperature. Up to time-step 200, the temperature increases smoothly, predominantly by diffusion. At time-step 200, the abrupt increase in temperature indicates that advection has become an important transport process (at least locally). By time-step 300, almost exactly one rotation after start, the temperature has reached a maximum value and starts to oscillate with irregular amplitude and period. Beyond time-step 450, the oscillations of w and T are almost coherent. This indicates that advection dominates heat transfer beyond time-step 450 at this particular location.

Figure 10(*a*) shows the two-dimensional development of instability 2.5 rotations

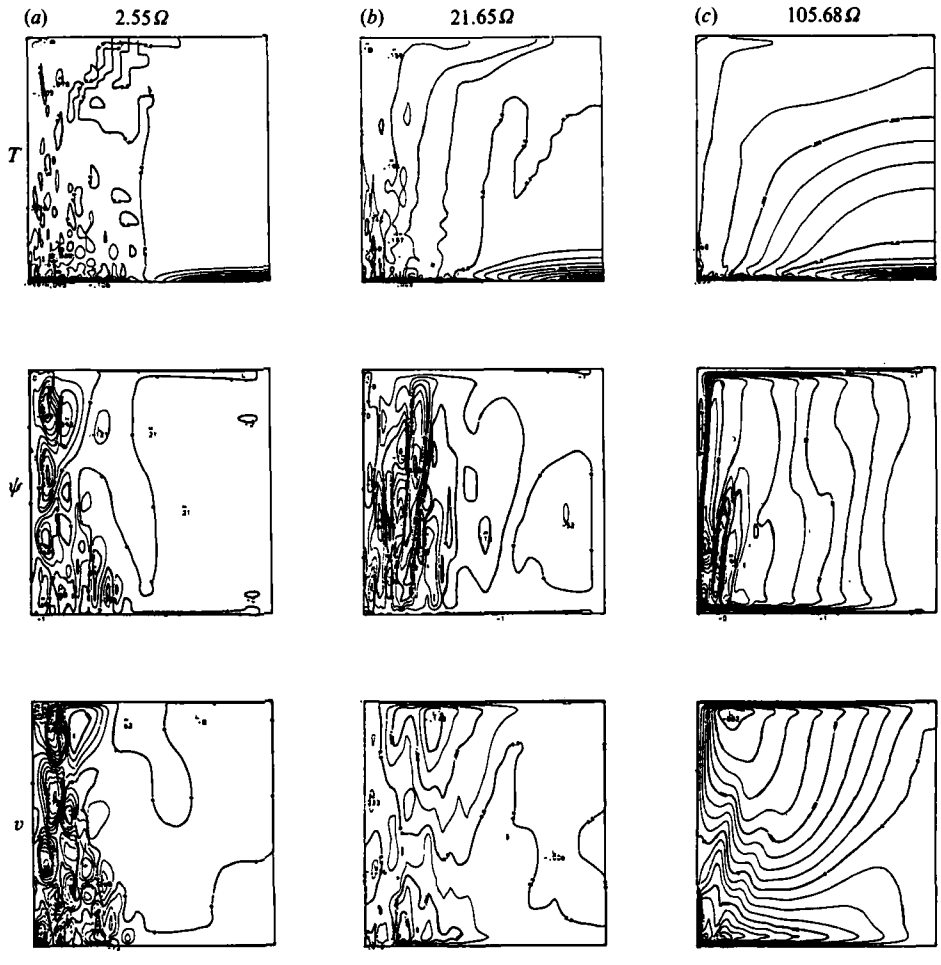

FIGURE 10. Time-dependent development of case 5, towards quasi-steady state. Time in rotations.

after the computation had started (1 rotation = 4π dimensionless time). After heating is switched on, the initial heat transfer is by conduction. Within half a rotation, while the thermal layer is still very thin, ≈ 0.02 dimensionless units ($\frac{1}{50}$ of the cavity width), unstable cells of the lengthscale of the thermal-layer thickness start to appear, without disturbing the isotherms. This is the first stage of instability at time-step 200 (0.64Ω) as shown in figure 9 (a, b). Because this stage of instability takes place about half a rotation after the heating start, it is safe to assert that this stage of instability is totally thermally controlled (i.e. rotation has not played an effective roll). Howard (1966) had made an estimate of the effective Rayleigh number at the onset of thermal instability for a deep layer of fluid without rotation. His critical Rayleigh number is about 2500, which is close to our estimate here. A detailed discussion of the onset of instability is given in a subsquent paper (Quon 1987).

The first stage of instability is confined to the bottom boundary layer and lasts less than one rotation. The next stage of instability entails cellular penetration into the upper part of the unstable half of the cavity in the form of breaking thermals. Isolated thermals start to form and to break off the thermal layer. The penetrative

processes spread towards the fluid interior from the vertical boundary, and take on multiple vertical wavenumbers. Initially the number of vertical cells decreases with distance from the boundary (figure 10*a*, Ψ-frame). This reflects the fact that the Rayleigh numbers decrease with x, and according to D & S's theory, the largest number of vertical cells should occur where the largest Rayleigh number is, which is next to the vertical boundary. At the peak of this stage of instability, the whole left-hand side of the cavity is filled with almost randomly distributed cells. However the vertical stacks of cells are recognizable as shown in figure 10(*a*). The aspect ratios of the cells range from 1 to 2. Note that at this stage, while the left-hand side of the cavity is almost turbulent, the thermally stable half of the cavity has only weak and orderly motion. The evolution from the peak of almost chaotic motion to quasi-steady state is depicted in figure 10(*b*, *c*). It is quite obvious that the cells coalesce in the vertical into a few tall and thin cells as shown in the stream function of figure 10(*c*). The isotherms become almost vertical in the left half of the cavity. In the meantime the rest of the fluid has organized into strong Ekman layers near the top and bottom boundaries which create Ekman suction in the interior. Since the heat transfer of this case is extremely nonlinear, the left-hand side of the cavity eventually becomes almost isothermal owing to vigorous advection. Consequently the vertical temperature gradient becomes very weak, and the Rayleigh number becomes very small. At steady state or quasi-steady state, the Rayleigh number is no longer strong enough to sustain cellular motion (figure 3*e*).

To summarize, we have observed that the transient states are much more sensitive to the variation of β than the steady states. Thus case 1 and case 2 may have very similar steady states, but their approaches to these states differ markedly from each other. Case 2 and case 3 both have transient cellular states, but the cells are initiated under very different conditions. For case 2, cellular motions appear about 146 rotations after heating start. It appears that the $E^{\frac{1}{3}}$ side layer has already fully developed when these cells form. Although these cells can persist for a very long time, over 1050 rotations they have finally dissipated, and in case 2 reach a steady state similar to that of case 1, a one-cell circulation. On the other hand, the cellular instability for case 3 takes place quite early in the computation, about 9.5 rotations after the heating start. By rotation 50, the cells have fully developed into full strength. Although the number of cells had decreased from five at the peak of activity to three at steady state, the Rayleigh number at steady state was sufficiently large to maintain three boundary cells permanently. It should be noted that throughout the whole transient development, cells only have vertical wavenumber unity for case 3. In other words, according to linear theory, the Rayleigh number is never large enough to support a vertical wavenumber greater than unity.

At yet higher values of β such as those of cases 4 and 5, thermal instability starts very early, within half of a rotation after the heating start. Individual thermals randomly form and rapidly detach from the thermal layer to penetrate into the fluid immediately above. The cellular motions become very vigorous within the entire unstable side of the cavity. These cells have dominant vertical wavenumbers of 4 and 5. The most amazing phenomenon is that while almost turbulent motion is displayed in the thermally unstable half of the cavity, the adjacent half to the right remains quiescent with very orderly motion. Through vigorous advection and ever-present diffusion, the unstable region eventually becomes almost isothermal, and thus the Rayleigh number becomes too small to sustain any cellular motion. A one-cell circulation prevails in a steady or quasi-steady state. It appears that because the heating is so strong for both cases 4 and 5, instability takes place almost immediately

after the heat is switched on. This happens before the side layer is formed, or before the rotational effect has been firmly established, although rotation plays a strong role later in the development. There are also differences between case 4 and case 5. The former attains a steady state, while the latter undergoes very persistent, low-amplitude oscillations which have emanated from the unstable lower corner and propagated throughout the whole cavity.

We have only been able to present the bare essentials of the transient flows here. The rich and complex motion can be fully appreciated only through viewing a computer movie.

10. Discussion

We have studied the transient states, steady states and quasi-steady states of a rotating fluid in a rigidly bounded square which is differentially heated on the bottom boundary for a wide range of thermal Rossby numbers. For low thermal Rossby number, the numerical results confirm the linear and weakly nonlinear theories of D & S. At supercritical Rayleigh number, steady states exist, although these steady states differ markedly from one another, depending on the thermal Rossby number. The existence of these final states shows that the instability is an exchange instability rather than a catastrophic one. This has answered one of the important questions raised in D & S's analyses. Another question concerning bifurcation of the solutions has not been answered. Although there are jumps in the solutions (say from Bénard instability to multiple-vertical-wavenumber instability to a one-cell steady state), it is not clear whether there are other possible states. It is felt that other states are unlikely if computations are limited to two space dimensions. Another observation in this study is that although the D & S theories cannot describe transient states in detail, they have provided some valuable insight into the multiple-vertical-wavenumber instability at different stages of the temporal development.

Daniels's (1976) question of whether it is necessary to have slightly conducting sidewalls in order to maintain steady flows has been answered in the negative. Cases 1–4 all have steady states with perfectly insulated sidewalls (apart from numerical truncation error). However, his conjecture on flows at high thermal Rossby number has been confirmed by the numerical results. D & S also raised doubt on the possibility of solving this problem numerically because the boundary layers are very thin, and therefore very hard to resolve. Although large computing resources are required, it is possible to resolve the boundary layers by coordinate transformation, at least for the two-dimensional problem. A three-dimensional problem would increase the resource requirement by two orders of magnitude.

Finally, it is worth pointing out that there is a common misconception that one should expect a symmetric flow in this problem because the imposed temperature on the bottom boundary is antisymmetric. While this is true for the conductive regime, it is not an adequate condition for symmetric flows in the convective regime. In order to have some kind of symmetry, say centro-symmetry or centro-antisymmetry about the centre of the cavity (Gill 1966), in all the steady fields in a convection problem, one must impose the *same* temperature (symmetric conditions, Quon 1977, 1980), or *reverse* temperature (antisymmetric conditions, Quon 1972, 1983*a*, *b*) on the *opposite* boundaries, although the temperatures themselves need not assume any specific functional form along the boundaries. This holds true for systems with or without rotation.

All the computations presented in this paper were done at NCAR, Boulder, while I was on leave from Bedford Institute. I wish to thank all my colleagues in AAP, in particular those in the oceanography section, and all the consultants in SCD at NCAR for their hospitality and assistance. NCAR is supported by NSF. A computer movie of all the transient states reported in this paper ($\frac{1}{2}$ hour long) can be loaned from the author for viewing.

I had benefited from a long, amiable, and encouraging conversation with Professor Keith Stewartson on this particular problem. I wish to dedicate this paper to his memory.

Appendix

Starting from (7.1*c*), we observe that:

$$T = F(\Psi), \tag{A 1}$$

where $F(\Psi)$ is an arbitrary function of Ψ. Combining (7.1*a*, *b*), and (A 1) we have

$$E^2\nabla^6\Psi + \frac{\partial^2\Psi}{\partial z^2} + E\nabla^2\frac{\partial F(\Psi)}{\partial x} = 0. \tag{A 2}$$

Since $F(\Psi)$ is an arbitrary function of Ψ, (A 2) can be nonlinear. In order to make (A 2) analytically tractable so that we can gain some insight into the nature of the boundary layer, we consider T as a linear function of Ψ, i.e.

$$T = F(\Psi) = 2A\Psi + B, \tag{A 3}$$

where A and B are arbitrary constants. Note that by reducing the temperature equation from second- to first-order in (7.1*c*), we are able to apply only one boundary condition to the temperature in the x- and one in the z-direction. We shall be able to determine only A or B because we have only one boundary condition in x for the temperature at our disposal when we consider the boundary-layer equations.

Substituting (A 3) into (A 2), we obtain

$$E^2\nabla^6\Psi + \frac{\partial^2\Psi}{\partial z^2} + 2AE\nabla^2\frac{\partial\Psi}{\partial x} = 0. \tag{A 4a}$$

By scaling $x = E^{\frac{1}{3}}\xi$, (A 4*a*) becomes

$$\frac{\partial^6\Psi}{\partial\xi^6} + \frac{\partial^2\Psi}{\partial z^2} + 2A\frac{\partial^3\Psi}{\partial\xi^3} = O(E^{\frac{2}{3}}\Psi) + O(AE^{\frac{2}{3}}\Psi). \tag{A 4b}$$

In order that all terms on the left-hand side play equal roles, we assume $A = O(1)$.

By replacing x with the stretched coordinate ξ in (7.1*a*, *b*), we have

$$\frac{\partial v}{\partial z} = E^{-\frac{1}{3}}\frac{\partial T}{\partial\xi} + E^{-\frac{1}{3}}\frac{\partial^4\Psi}{\partial\xi^4}, \tag{A 5a}$$

$$-\frac{\partial\Psi}{\partial z} = E^{\frac{1}{3}}\frac{\partial^2 v}{\partial\xi^2}. \tag{A 5b}$$

We note that T and Ψ must be $O(E^{\frac{1}{3}}v)$ in order for all terms in these equations to balance one another. For convenience we define

$$T = E^{\frac{1}{3}}\theta, \quad \Psi = E^{\frac{1}{3}}\phi,$$

where $\theta, \phi = O(v)$, and ϕ still satisfies (A 4b) which admits solutions of the form

$$\phi = \phi_0 + \sum_{m=1}^{\infty} \phi_m \, e^{\lambda_m \xi} \sin(m\pi z). \tag{A 6}$$

For each m, we have

$$\lambda_m^6 + 2A\lambda_m^3 - (m\pi)^2 = 0. \tag{A 7}$$

There are 6 roots for λ_m. In order to have boundary-layer-type solutions, we are looking for three roots with negative real parts so that the solutions will be bounded and approach an asymptotic value ϕ_0 as $\xi \to \infty$. Three roots are sufficient to give three free constants so that the first three boundary conditions in (7.2) are satisfied. This may impose a condition on A. From (A 7), we find

$$(\lambda_{m\pm}^3) = -A \pm (A^2 + (m\pi)^2)^{\frac{1}{2}}, \tag{A 8}$$

where the right-hand side is real because A and m are real. Hence λ_m^3 are real.

When $\lambda_m^3 > 0$, one of the roots of λ_m has positive real part, and *two* have negative real parts. When $\lambda_m^3 < 0$, *one* root has negative real part and two have positive real parts. Therefore *regardless of the value of* A, *we can always find three roots of* λ *in* (A 7) *with negative real parts* to form a boundary layer that can satisfy all boundary conditions in (7.2). The boundary layer is of the form

$$\phi = \phi_0 + \sum_{m=1}^{\infty} \sin(m\pi z)\,(\phi_{m,1} \, e^{\lambda_{m,1}\xi} + \phi_{m,2} \, e^{\lambda_{m,2}\xi} + \phi_{m,3} \, e^{\lambda_{m,3}\xi}). \tag{A 9}$$

Now if we let $G_1^3 = A + [A^2 + (m\pi)^2]^{\frac{1}{2}}$, and $G_2^3 = -A + [A^2 + (m\pi)^2]^{\frac{1}{2}}$, then $\lambda_{m,1} = -G_1, \lambda_{m,2} = -(\frac{1}{2}G_2)(1 - i\sqrt{3}), \lambda_{m,3} = -(\frac{1}{2}G_2)(1 + i\sqrt{3})$, where $i = \sqrt{-1}$.

Since ϕ is real, without loss of generality we can rewrite (A 9) as

$$\phi = \phi_0 - \sum_{m=1}^{\infty} \sin(m\pi z)\left(C_m \, e^{-G_1\xi} + e^{-\frac{1}{2}G_2\xi}\left(D_m \sin\frac{\sqrt{3}}{2}G_2\xi + E_m \cos\frac{\sqrt{3}}{2}G_2\xi\right)\right) \tag{A 10a}$$

$$v = v_0 + \sum_{m=1}^{\infty} m\pi \cos(m\pi z)\left[\frac{C_m}{G_1^2} e^{-G_1\xi} + \frac{1}{G_2^2} e^{-\frac{1}{2}G_2\xi}\left(D_m \sin\left(\frac{\sqrt{3}}{2}G_2\xi + \frac{2\pi}{3}\right) + E_m \cos\left(\frac{\sqrt{3}}{2}G_2\xi + \frac{2\pi}{3}\right)\right)\right], \tag{A 10b}$$

where C_m, D_m, E_m are real constants, and ϕ_0 and v_0 are asymptotic values of ϕ and v as $\xi \to \infty$. Applying (7.2) to (A 10), we have

$$\left.\begin{aligned} &\sum_{m=1}^{\infty} \sin(m\pi z)\,(C_m + E_m) = \phi_0 \quad \text{by } \phi = 0 \quad \text{at } \xi = 0, \\ &2\frac{G_1}{G_2}C_m - \sqrt{3}D_m + E_m = 0 \quad \text{by } \frac{\partial\phi}{\partial\xi} = 0 \quad \text{at } \xi = 0, \\ &\sum_{m=1}^{\infty} m\pi \cos(m\pi z)\left[\frac{C_m}{G_1^2} + \frac{1}{G_2^2}\left(D_m \sin\frac{2\pi}{3} + E_m \cos\frac{2\pi}{3}\right)\right] \\ &\qquad = -v_0 \quad \text{by } v = 0 \quad \text{at } \xi = 0. \end{aligned}\right\} \tag{A 11}$$

It is clear that unless ϕ_0 and v_0 are known, we cannot evaluate C_m, D_m and E_m. Therefore for definiteness, let us assume $\phi_0 = \phi^{\mathrm{I}}(0) =$ constant and $v_0 = v^{\mathrm{I}}(0, z)$,

which is some function of z as the thermal wind balance in the interior would require. Thus we have

$$C_n + E_n = \frac{4\phi_0}{(2n+1)\pi}$$

where $n = \frac{1}{2}(m-1), n = 0, 1, 2, \ldots$ and

$$\sum_{n=0}^{\infty} (2n+1)\pi \cos[(2n+1)\pi z] C_n \frac{G_1^3 + G_2^3}{G_1^2 G_2^3} = -v^{\mathrm{I}}(0, z).$$

If we further assume that we can write

$$v^{\mathrm{I}}(0, z) = -\sum_{n=0}^{\infty} \hat{v}_n \cos(2n+1)\pi z, \tag{A 12}$$

we have

$$C_n = \frac{G_1^2 G_2^3}{G_1^3 + G_2^3} \frac{\hat{v}_n}{(2n+1)\pi},$$

$$E_n = \frac{4\phi_0}{(2n+1)\pi} - C_n,$$

$$D_n = \frac{\sqrt{3}}{3}\left[(2G_1 - G_2)\frac{C_n}{G_2} + \frac{4\phi_0}{(2n+1)\pi}\right],$$

and

$$\Psi = E^{\frac{1}{3}}\left[\phi_0 - \sum_{n=0}^{\infty} \sin(2n+1)\pi z \left(C_n \mathrm{e}^{-G_1\xi} + \mathrm{e}^{-\frac{1}{2}G_2\xi}\left(D_n \sin\frac{\sqrt{3}}{2} G_2\xi + E_n \cos\frac{\sqrt{3}}{2} G_2\xi\right)\right)\right], \tag{A 13a}$$

$$v = v_0 + \sum_{n=0}^{\infty} (2n+1)\pi \cos(2n+1)\pi z \left[\frac{C_n}{G_1^2} \mathrm{e}^{-G_1\xi} + \frac{1}{G_2^2} \mathrm{e}^{-\frac{1}{2}G_2\xi}\left(D_n \sin\left(\frac{\sqrt{3}}{2} G_2\xi + \frac{2\pi}{3}\right) + E_n \cos\left(\frac{\sqrt{3}}{2} G_2\xi + \frac{2\pi}{3}\right)\right)\right], \tag{A 13b}$$

$$T = 2AE^{\frac{1}{3}}\left[\phi_0 - \sum_{n=0}^{\infty} \sin(2n+1)\pi z \left(C_n \mathrm{e}^{-G_1\xi} + \mathrm{e}^{-\frac{1}{2}G_2\xi}\left(D_n \sin\frac{\sqrt{3}}{2} G_2\xi + E_n \cos\frac{\sqrt{3}}{2} G_2\xi\right)\right)\right] + B. \tag{A 13c}$$

Now we can choose an appropriate boundary condition for T. Since $\phi_\xi = 0$ at $\xi = 0$, from (A 3) $T_\xi = E^{\frac{1}{3}} B_x = 0$ is automatically satisfied. If we apply the asymptotic condition that $T \to T^{\mathrm{I}}(0)$, as $\xi \to \infty$, then

$$T^{\mathrm{I}}(0) = 2AE^{\frac{1}{3}}\phi_0 + B, \quad \text{or } B = T^{\mathrm{I}}(0) - 2AE^{\frac{1}{3}}\phi_0 = \text{constant}.$$

Hence

$$T = T^{\mathrm{I}}(0) - 2AE^{\frac{1}{3}} \sum_{n=0}^{\infty} \sin(2n+1)\pi z \times \left(C_n \mathrm{e}^{-G_1\xi} + \mathrm{e}^{-\frac{1}{2}G_2\xi}\left(D_n \sin\frac{\sqrt{3}}{2} G_2\xi + E_n \cos\frac{\sqrt{3}}{2} G_2\xi\right)\right) \tag{A 13d}$$

The constant A in (A 13d) cannot be determined, although we know that $A = O(1)$. Hence the second term on the right-hand side of (A 13d) is $O(E^{\frac{1}{3}})$ smaller than the interior temperature T^{I} which is $O(1)$.

Despite the fact that we have made a number of assumptions to arrive at these

boundary-layer solutions, they bear some quantitative resemblance to the numerical solutions. For example, if $T^I(0) = 0.5$, the maximum possible temperature of the system, the boundary-layer correction is $O(E^{\frac{1}{3}}) = 0.05$, about 10% of $T^I(0)$. Figure 4 shows that $T(0, z) \approx 0.45$ for case 5. By $w = \partial\Psi/\partial x = \partial\phi/\partial\xi$, we have $w = O(v(0))$, and the e-folding distance of the boundary layer is $O(E^{\frac{1}{3}})$. Qualitatively both T and Ψ have extrema at $z = \frac{1}{2}$, while v has a zero somewhere between $z = 0$ and 1. All these are borne out by the numerical solutions if we compare them with figure 3.

This boundary layer is similar to that of the linear theory given in (4.4a) in some respects; both have lengthscale $E^{\frac{1}{3}}$. However, in the linear theory boundary-layer solutions are possible only if the internal Rayleigh number is less than critical. But there is no such restriction here because strong advection makes the boundary region almost isothermal, and $\partial T_0/\partial z$ is always positive in the interior. Therefore a boundary-layer solution always exists under the present assumptions. This aspect of the solution is indeed what we have intended to establish. We cannot ascertain that it must exist because of the assumptions we have made, although these assumptions are reasonable ones and are supported by the numerical solutions.

REFERENCES

Beardsley, R. C. & Festa, J. F. 1972 A numerical model of convection driven by a surface stress and non-uniform horizontal heating. *J. Phys. Oceanogr.* **2**, 444–455.

Chandrasekhar, S. 1962 *Hydrodynamic and Hydromagnetic Stability.* Oxford University Press.

Daniels, P. G. 1976 Thermal convection in a differentially heated rotating fluid annulus. *Geophys. Fluid Dyn.* **7**, 297–330.

Daniels, P. G. & Stewartson, K. 1977 On the spatial oscillations of a horizontally heated rotating fluid. *Math. Proc. Camb. Phil. Soc.* **81**, 325–349.

Daniels, P. G. & Stewartson, K. 1978 On the spatial oscillations of a horizontally heated rotating fluid. II. *Q. J. Mech. Appl. Maths* **31**, 113–135.

Gill, A. E. 1966 The boundary layer regime for convection in a rectangular cavity. *J. Fluid Mech.* **26**, 515–536.

Hignett, P., Ibbetson, A. & Killworth, P. D. 1981 On rotating thermal convection driven by non-uniform heating from below. *J. Fluid Mech.* **109**, 161–187.

Howard, L. N. 1966 Convection at high Rayleigh number. *Proc. 11th Intl congr. of applied mechanics, Munich 1964* (ed. H. Gortler), pp. 1109–1115. Springer-Verlag.

Hunter, C. 1967 The axisymmetric flow in a rotating annulus due to a horizontally applied temperature gradient. *J. Fluid Mech.* **27**, 753–778.

Kalnay de Rivas, E. 1973 Numerical models of the circulation of the atmosphere of Venus. *J. Atmos. Sci.* **30**, 763–779.

Killworth, P. D. & Manins, P. C. 1980 A model of confined thermal convection driven by non-uniform heating from below. *J. Fluid Mech.* **98**, 587–607.

Needler, G. T. 1967 A model for thermocline circulation in an ocean of finite depth. *J. Mar. Res.* **25**, 329–342.

Quon, C. 1972 High Rayleigh number convection in an enclosure – a numerical study. *Phys. Fluids* **15**, 12–19.

Quon, C. 1976 A mixed spectral and finite difference model to study baroclinic annulus waves. *J. Comp. Phys.* **29**, 442–479.

Quon, C. 1977 Axisymmetric states of an internally heated rotating annulus. *Tellus* **29**, 83–96.

Quon, C. 1980 Quasi-steady symmetric regimes of a rotating annulus differentially heated on the horizontal boundaries. *J. Atmos. Sci.* **37**, 2407–2423.

Quon, C. 1981 In search of symmetric baroclinic instability in an enclosed rotating fluid. *Geophys. Astrophys. Fluid Dyn.* **17**, 171–197.

Quon, C. 1983a Effect of grid distribution on the computation of high Rayleigh number

convection in a differentially heated cavity. In *Numerical Properties and Methodologies in Heat Transfer* (ed. T. M. Shih), pp. 261–281. Hemisphere and Springer.

QUON, C. 1983*b* Convection induced by insulated boundaries in a square. *Phys. Fluids* **26**, 632–637.

QUON, C. 1986 Temporal development of spatial oscillations in a confined rotating fluid – a numerical study. *Geophys. Astrophys. Fluid Dyn.* **36**, 207–228.

QUON, C. 1987 Onset of spatial oscillations in a deep rotating fluid differentially heated from below. *Phys. Fluids* **30**, 672–678.

ROBERTS, G. O. 1971 Computational meshes for boundary layer problems. In *Proc. Second Intl Conf. on Numerical Methods in Fluid Dynamics* (ed. M. Holt), pp. 171–177. Springer.

ROBINSON, A. R. 1959 The symmetric state of a rotating fluid differentially heated in the horizontal. *J. Fluid Mech.* **6**, 599–620.

ROSSBY, H. T. L. 1965 On thermal convection driven by non-uniform heating from below: an experimental study. *Deep-Sea Res.* **12**, 9–16.

STERN, M. E. 1975 Horizontal convection and thermoclines. In *Ocean Circulation Physics*, Ch. 12. Academic.

STEWARTSON, K. 1957 On almost rigid rotation. *J. Fluid Mech.* **3**, 17–26.

STOMMEL, H. 1962 On the smallness of sinking regions in the ocean. *Proc. Nat. Acad. Sci.* **48**, 766–772.